Energy.Equip.Sys./ Vol. 13/No. 3/September 2025/211-227

Energy Equipment and Systems

www.energyequipsys.com

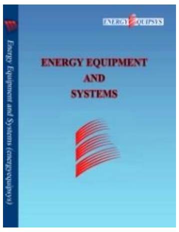

CFD-based multi-objective optimization of impinging jet ventilation (IJV) systems to improve the local indoor air quality (IAQ) indexes

Manuscript Type
Research Paper

Authors

Hamed Shaker Taheri [a]
Behrang Sajadi [a*]

[a] School of Mechanical Engineering, College of Engineering, University of Tehran, Tehran, Iran.

Article history:

Received: 12 January 2025
Revised: 17 February 2025
Accepted : 27 March 2025

ABSTRACT

Impinging jet ventilation (IJV) systems, despite some advantages, encounter certain weaknesses in delivering local thermal comfort and detachment of particles from the floor. This study utilizes the NSGA-II algorithm to optimize the design parameters of IJV systems, aiming to achieve optimal conditions for thermal comfort and particle suspension. In this context, a surrogate model based on an artificial neural network (ANN) coupled with computational fluid dynamics (CFD) is employed to explore the problem space. The Jonson-Kendall-Roberts (JKR) model is also implemented using a UDF in Fluent software to simulate particle detachment from the ground level. The optimization variables encompass the dimensions of the air inlet nozzle, the nozzle height, the mass flow rate of the nozzle inlet, and the objective functions comprise the vertical temperature difference, draft index, and the total residence time of suspended particles within the room space. A factorial analysis was performed to evaluate the influence of design variables on the objective functions. The analysis revealed that all design variables have a significant impact on the performance of impinging jets in achieving the desired objective functions. Mass flow rate emerged as the most influential parameter, exerting the strongest effect on the optimized objective functions. After optimization, the points $X = 0.14\ m$, $Z = 0.17\ m$, $H = 1.19\ m$, $\dot{m} = 0.034\ kg\ s^{-1}$ *are chosen from the Pareto front as the consensus optimal point with more favorable objective functions compared to other options.*

Keywords: Impingement Jet Ventilation (IJV); Particle Detachment; Indoor Air Quality (IAQ); Thermal Comfort; Artificial Neural Network (ANN).

1. Introduction

In today's world, heating, ventilation, and air conditioning (HVAC) systems have become indispensable and wield a profound influence on both our well-being and productivity. This challenge has caused the development of innovative ventilation solutions for indoor environments. One such technique is impinging jet ventilation (IJV), conceived by Karimpanah and Awbi [1]. This method utilizes a high-velocity stream of air that impinges upon the floor, dispersing across the surface and effectively ventilating the designated space. A wide range of research has been conducted on IJV, with a particular emphasis on comparing its

---

* Corresponding author: Behrang Sajadi
School of Mechanical Engineering, College of Engineering, University of Tehran, Tehran, Iran
Email: bsajadi@ut.ac.ir

performance to other ventilation methods. Research by Karimpanah and Awbi [2] explored the benefits of IJV against older methods like displacement and mixing ventilation. In a study by Ye et al. [3], researchers compared the concentration of contaminants under both IJV and mixing ventilation methods. Their findings revealed that the IJV system provides a more favorable environment for managing contaminant distribution compared to mixing ventilation. Meanwhile, Chen et al. [4] leveraged simulations to compare the performance of four ventilation techniques within a room under identical temperature conditions and evaluated factors including thermal comfort, ventilation effectiveness, and energy consumption. This research indicated that the impinging jet ventilation method provides a better distribution of age of air and predicted mean vote (PMV) index. However, it exhibits deficiencies in local thermal comfort, particularly regarding vertical temperature difference and draft. Additionally, a major drawback of IJV systems is the issue of particle resuspension within the space. A high-velocity air jet impinging on the floor has a high potential for dislodging particles. In a study by Zuo et al. [5], researchers compared the concentration of particle resuspension in IJV and displacement ventilation methods. Their findings revealed that displacement ventilation provides a more favorable environment for managing airborne particulate matter compared to IJV. Also, Zuo et al. [5] experimentally investigated the impact of nozzle height and airflow rate on particle resuspension in a room equipped with an impinging jet ventilation (IJV) system where a particle source is positioned beneath the IJV nozzle. They further compared the performance of IJV to displacement and mixed ventilation methods. One of the most significant findings of their study is the weakness of the IJV system in managing particle resuspension compared to other ventilation systems.

In recent years, a limited number of studies have investigated parameters influencing the design of IJV systems. Haghshenas et al. [6] examined the impact of a ceiling exhaust on thermal comfort conditions and the age of air. They concluded that using a ceiling exhaust improves the performance of IJV. Chen et al. [7] investigated the influence of nozzle shape, nozzle height, nozzle flow rate, and the supply air temperature on ventilation comfort indexes. They found that the flow rate has the most significant impact on the draft index. In another research work, Chen et al. [8] conducted a study to investigate the impact of different thermal loads on indoor air distribution. Ye et al. [9] studied the effect of nozzle height, nozzle area, and nozzle outlet temperature on the hot air diffusion length in a room equipped with IJV. The optimal values to maximize the diffusion length were determined. Haghshenas et al. [10] optimized IJV performance using the Taguchi method. In this optimization, nozzle outlet temperature, return air inlet height, and percentage of air discharged from the ceiling exhaust were considered. The objective functions of the optimization process were thermal comfort indexes, age of air, and energy consumption. Wang et al. [11] evaluated the effect of nozzle length, width, and height on heat removal effectiveness and dimensionless buoyant jet length. Their results showed that increasing the three geometric parameters of the nozzle improves heat removal. Li et al. [12] optimized the removal of exhaled particles in the IJV and investigated the effect of inlet air parameters on the dispersion of exhaled particles.

As mentioned earlier, the main weaknesses of IJV systems are their potential to detach particles from the floor and their tendency to increase local thermal discomfort due to draft and vertical temperature difference. A review of existing literature reveals that a few research works have focused on particle dispersion in IJV systems. Furthermore, among the relatively few studies that have examined the behavior of particles in IJV, none have explored the detailed mechanism of particle detachment from the floor. Besides, among the optimization studies conducted on IJV systems, none have comprehensively explored the impact of IJV nozzle geometric specifications and airflow rate using optimization variables and suspended particles as the optimization objective function. Based on previous research works, the main weaknesses of the IJV system are the resuspension of particles from the floor as well as the risk of local thermal discomfort. Additionally, the inlet nozzle design parameters have the greatest impact on the selected objective functions. Therefore, this study aims to optimize the performance of the IJV system by minimizing three key parameters: total suspended particle residence time, vertical air temperature difference, and draft index. To achieve this, the nozzle dimensions, nozzle height, and discharge airflow rate are employed as optimization variables. By optimizing these parameters, the performance of the IJV system is expected to improve as its weaknesses are mitigated. For this purpose, a surrogate neural network model is used to reduce the computational costs. In addition, the JKR model is employed to estimate the shear criteria for particle resuspension from the surfaces. Subsequently, the NSGA-II optimization method is applied to evaluate the optimal points. In this study, particles are placed on the ground and are separated from the ground, and enter the simulation environment if the conditions for their separation and suspension from the ground are met. The conditions for separating particles from the floor are applied using a UDF based on existing particle separation theories. In this study, a neural network is used to create a surrogate model of the problem space that generates the problem's objective functions concerning the problem design variables to reduce computational costs. Subsequently, a multi-objective optimization is performed using the NSGA method. Another innovation used in this paper is the optimization algorithm, in which the neural network model obtained is updated and trained with new data using the optimal design points at each stage and other random points as the optimization progresses to reduce the error of the surrogate model.

Nomenclature

C_d	Drag coefficient (-)
d	Diameter (m)
g	Gravitational acceleration (m s^{-2})
F_{po}	Pull-off force (kg m s^{-2})
K	Young's modulus (kg m^{-1} s^{-2})
k	Turbulent kinetic energy (m^{2} s^{-2})
m	Mass (kg)
N	Number of asperities per unit area (m^{-2})
n	Number of resuspended particles (-)
Pr	Prantl number (-)
Re	Reynolds number (-)
T	Temperature (K)
T'	Temperature fluctuation (K)
t_r	Total residence time (s)
V	Velocity magnitude (m^{2} s^{-1})
u	Velocity (m s^{-1})
u'	Velocity fluctuation (m s^{-1})
u^*	Shear velocity (m s^{-1})
W_a	Work of adhesion (kg s^{-2})
Greek	
β	Coefficient of thermal expansion (K^{-1}), Asperity radius (m)
Δ_c	Roughness parameter (-)
δ_c	Maximum extension of asperities parameter (m)
δ_{ij}	Dirac delta function (-)
ε	Dissipation rate of turbulent kinetic energy (m^{2} s^{-3})
Γ	Diffusion coeficient (m s^{-2})
μ	Dynamic viscosity (m^{2} s^{-1})
ν	Kinematic viscosity (m^{2} s^{-1})
ρ	Density (kg m^{-3})
σ	Standard deviation (m)
τ_r	Relaxation time (s)
Subscript	
p	Particle

2. Materials and Methods

2.1. Governing equations

2.1.1. Airflow

In this study, the flow is assumed steady-state, three-dimensional, incompressible, and turbulent. The buoyancy force is implemented using the Boussinesq approximation. Using the Reynolds-averaged Navier-Stokes (RANS) equations for the airflow field [13]:

The continuity equation is:

$$\frac{\partial u_i}{\partial x_i} = 0 \tag{1}$$

The momentum equations are:

$$u_j \frac{\partial u_i}{\partial x_j} = -\frac{1}{\rho}\frac{\partial P}{x_i} + \frac{\partial}{\partial x_j}\left(\nu \frac{\partial u_i}{\partial x_j} - \overline{u_i' u_j'}\right) + \beta g (T - T_0) \tag{2}$$

The energy equation is:

$$u_j \frac{\partial T}{\partial x_j} = \frac{\partial}{\partial x_j}\left(\frac{\nu}{Pr}\frac{\partial T}{\partial x_j} - \overline{u_j' T'}\right) \tag{3}$$

In the above equations, u_i and T is the mean velocity and temperature, respectively. Also, u_i' and T' are, respectively, the velocity and temperature fluctuations. ρ, ν, Pr, and β are the air density, kinematic viscosity, Prandtl number, and thermal expansion coefficient are the reference working temperature, T_0, respectively.

This study employs ANSYS Fluent software for computational fluid dynamics (CFD) simulations. A second-order discretization scheme is implemented, and the SIMPLE method is employed for pressure-velocity coupling.

2.1.2. Turbulence modeling

There are various mathematical approximation methods to calculate turbulent stress $(-\overline{u_i'u_j'})$ and heat flux $(-\overline{u_j'T'})$ terms. Using the Boussinesq hypothesis and eddy viscosity concept:

$$-\overline{u_i'u_j'} = \nu_t\left(\frac{\partial u_i}{\partial x_j} + \frac{\partial u_j}{\partial x_i}\right) - \frac{2}{3}k\delta_{ij} \tag{4}$$

$$-\overline{u_j'T'} = \frac{\nu_t}{Pr_t}\left(\frac{\partial T}{\partial x_j}\right) \tag{5}$$

Two-equation models estimate the turbulence viscosity by solving two partial differential equations. Among these models, in this study, the RNG k-ε method is used which previous studies showed can provide acceptable results for indoor air distribution [13]:

$$\nu_t = C_\mu \frac{k^2}{\varepsilon} \tag{6}$$

where $C_\mu = 0.0845$ is a constant and k and ε are the turbulent kinetic energy and the turbulent dissipation rate, respectively, whose transport equations are [13]:

$$u_i \frac{\partial k}{\partial x_j} = \frac{\partial}{\partial x_j}\left(\alpha_k \nu_{eff} \frac{\partial k}{\partial x_j}\right) + P_k + P_b - \varepsilon \tag{7}$$

$$u_i \frac{\partial \varepsilon}{\partial x_j} = \frac{\partial}{\partial x_j}\left(\alpha_\varepsilon \nu_{eff} \frac{\partial \varepsilon}{\partial x_j}\right) + C_{1\varepsilon}\frac{\varepsilon}{k}(P_k + C_{3\varepsilon}P_b) - C_{2\varepsilon}\frac{\varepsilon^2}{k} - R_\varepsilon \tag{8}$$

in which $C_{1\varepsilon} = 1.42$, $C_{2\varepsilon} = 1.68$ are constants and ν_{eff} is the effective turbulent viscosity to better handle low Reynolds and near-wall flows. α_k and α_ε are the inverse effective Prandtl numbers for k and ε, respectively, which are calculated using RN theory. Also, P_k and P_b are the turbulent kinetic energy generation due to mean shear stress and buoyancy force, respectively, and R_ε represents the effect of flow strain rate on the dissipation rate [13,10].

2.1.3. Particles behavior

The focus of this study is on particle detachment and dispersion by the high-momentum airflow supplied by the impinging jet ventilation (IJV) system. As investigated particles are larger than 0.5 μm, the effects of Brownian motion and Saffman's force are negligible [13]. So, considering the drag and gravity forces on the particles [13]:

$$\frac{du_{i.p}}{dt} = \frac{u_i - u_{i.p}}{\tau_r} + g_i \tag{9}$$

where $u_{i.p}$ is the particle and m_p is its mass. Also, τ_r is the particle relaxation factor which is defined as [13]:

$$\tau_r = \frac{\rho_p {d_p}^2}{18\mu}\frac{24}{C_d Re_p} \tag{10}$$

where ρ_p and d_p are the particle density and its diameter, respectively. Also, Re_p is the particle Reynolds number:

$$Re_p = \frac{\rho_p d_p \left|u_i - u_{i,p}\right|}{\mu} \tag{11}$$

and C_d is the drag coefficient which is predicted using Morsi and Alexander [16].

To consider the effect of turbulence fluctuations on the motion of particles, the discrete random walk (DRW) model is used. For the $k - \varepsilon$ family turbulent models, the velocity fluctuations are modeled as:

$$u_i' = \varphi\sqrt{\frac{2k}{3}} \tag{12}$$

where φ is the normally distributed random function.

2.1.4. Particles detachment

In this study, a user-defined function (UDF) is employed to implement particle detachment from the ground surface. Whenever the detachment criterion is satisfied at a specific point on the ground, three particles are introduced into the corresponding cell and positioned near the ground. The critical shear velocity for particle detachment from rough surfaces was investigated in the study of Ahmadi and Soltani [14], which complemented the JKR model [15]. If the shear velocity at any point on the ground exceeds the calculated critical value, particles detach from the ground and enter the computational domain. In this study, to investigate the behavior of particles inside the room, four particle sizes, including 0.5, 1.5, 4.5, and 7.5 µm, are simulated.

The forces acting on a particle on a rough surface are shown in Fig. 1, F_{po} where the particle pull-off force, and F_t, F_l, and M_t are the drag force, lift force, and momentum induced by the near-wall turbulent airflow, respectively [16]:

$$F_t = 2.9\pi\rho u^{*2} d_p^2 \tag{13}$$

$$F_l = 0.97\rho u^{*3} d_p^3 \tag{14}$$

$$M_t = 1.07\pi\rho u^{*2} d_p^3 \tag{15}$$

where u^* is the wall shear velocity.

Johnson et al. [15] considered the effect of elastic deformation of particles to provide a model for particle detachment from smooth surfaces, named the Johnson-Kendall-Roberts (JKR) model. The KJR model was extended by Fuller and Tabor [17] to include the particle surface normally distributed asperities. Using the Fuller and Tabor model, Ahmadi and Sultani [16] investigated the detachment of particles from rough surfaces. Accordingly, the adhesive force acting on particles on rough surfaces is:

$$F_{po} = \pi a^2 N f_{po}\, exp\left(-\frac{0.6}{{\Delta_c}^2}\right) \tag{16}$$

where N is the number of asperities per unit area of the particle, and:

$$a = \frac{\pi}{2K} N f_{po} d_p\, exp\left(-\frac{0.6}{\Delta_c^2}\right) \tag{17}$$

where $K = 9.7 \times 10^{10}$ Pa is the composite Young's modulus of the particle. f_{po} is the adhesive force for each particle asperities:

$$f_{po} = \frac{3}{4}\pi W_A d_p \tag{18}$$

where W_A is the thermodynamic work of adhesion. Δ_c is the dimensionless roughness parameter of the surface which is defined as:

$$\Delta_c = \frac{\delta_c}{\sigma} \tag{19}$$

where σ is the standard deviation of the roughness distribution and δ_c is the maximum extension of asperities tips above their undeformed height:

$$\delta_c = \left(\frac{{f_{po}}^2}{3K^2\beta}\right)^{\frac{1}{3}} \tag{20}$$

where β is the asperity radius which assumed as $0.02d_p$ [16]. According to Greenwood and Williams [18] the relationship between N, β, σ is:

$$\beta\sigma N = 0.1 \tag{21}$$

Soltani and Ahmadi [16] noted that rolling is the most probable mechanism for particle detachment from rough surfaces. Using the angular momentum equation around the point "O", the critical shear velocity which leads to particle detachment due to the rolling mechanism is [16]:

$$u_c^* = \left[\frac{\pi a^3 N f_{po}\, exp\left(-\frac{0.6}{\Delta_c^2}\right)}{\rho d_p^3\left(2.52\pi + \frac{0.97 a u_c^*}{\upsilon}\right)}\right]^{0.5} \tag{22}$$

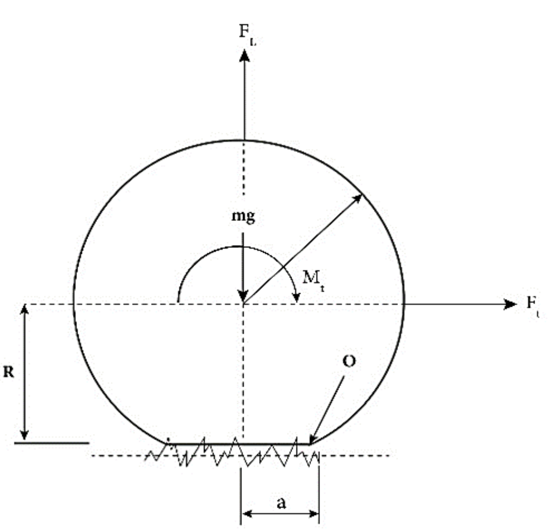

Fig. 1. Schematic of forces and momentums acting on a particle on a rough surface [16].

2.2. Geometry

Figure 2 depicts the modeled computational domain. The room is equipped with a jet impingement ventilation (IJV) system. Furthermore, the two sides of the air outlet nozzle, designated as X and Z, are marked in the figure. The boundary conditions employed in the are summarized in Table 1. Besides, ceiling cooling is employed to enhance comfort conditions.

2.3. Mesh independency

Three grids with 950,000, 2.6 million, and 4.9 million cells were compared. The meshes were generated using ANSYS Meshing software, and, in all cases, the value of y^+ was about 4, using the boundary layer mesh. The results showed that the maximum difference between temperature and velocity distribution results in the grids with 4.9 million and 2.6 million cells is less than 2% which indicates that the grid with 2.6 million cells is a suitable choice considering the computational cost optimization. It is worth mentioning that using the final grid reduced the computation time by up to 50% in comparison with the finest one.

2.4. Validation

The temperature and velocity distributions at A ($x = 2.1$ m, $y = 1.8$ m) and B ($x = 0.7$ m, $y = 0.3$ m) lines are compared with the experimental data of Chen et al. [7] experimental study in Fig. 3. The results showed that the simulation results are in good agreement with the experimental results. The normalized mean absolute errors are 8% and 6% for velocity and temperature results, respectively.

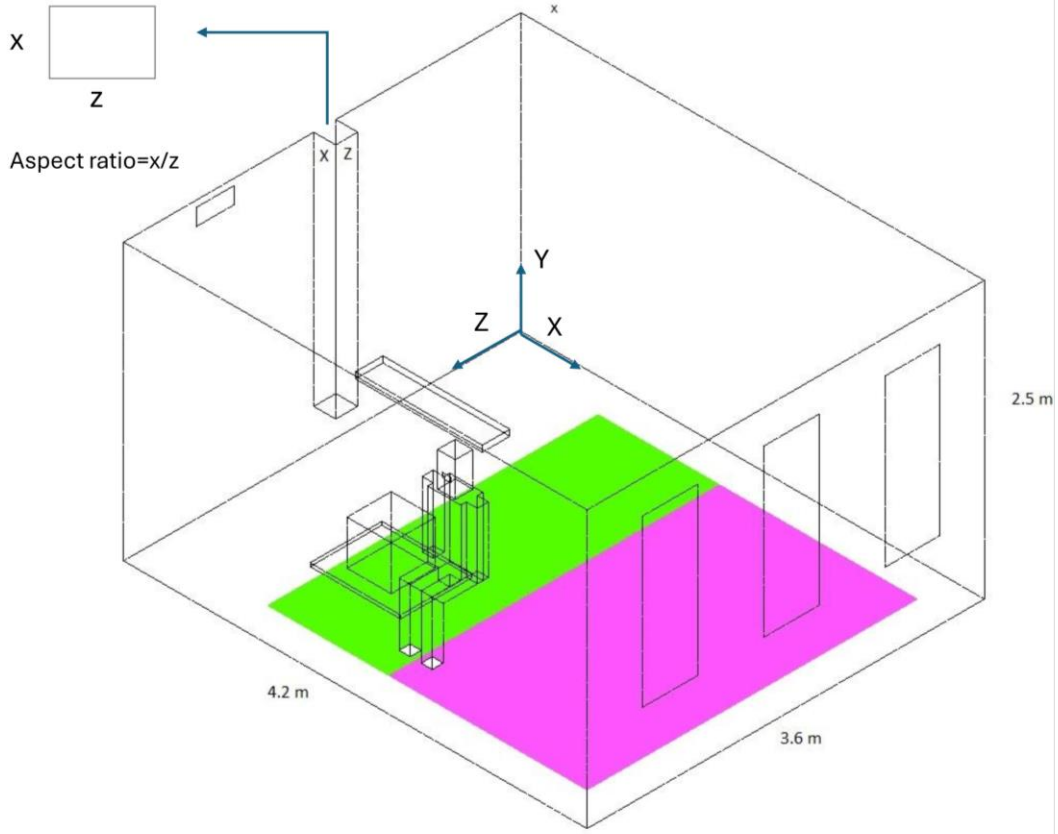

Fig. 2. Geometry of the studied office room equipped with the impinging jet ventilation (IJV).

Table 1. Heat release from the modeled room surfaces.

Surface	Window	Ceiling	Floor	Computer	Occupant	Light
Heat release (W)	110	230	150	120	100	60

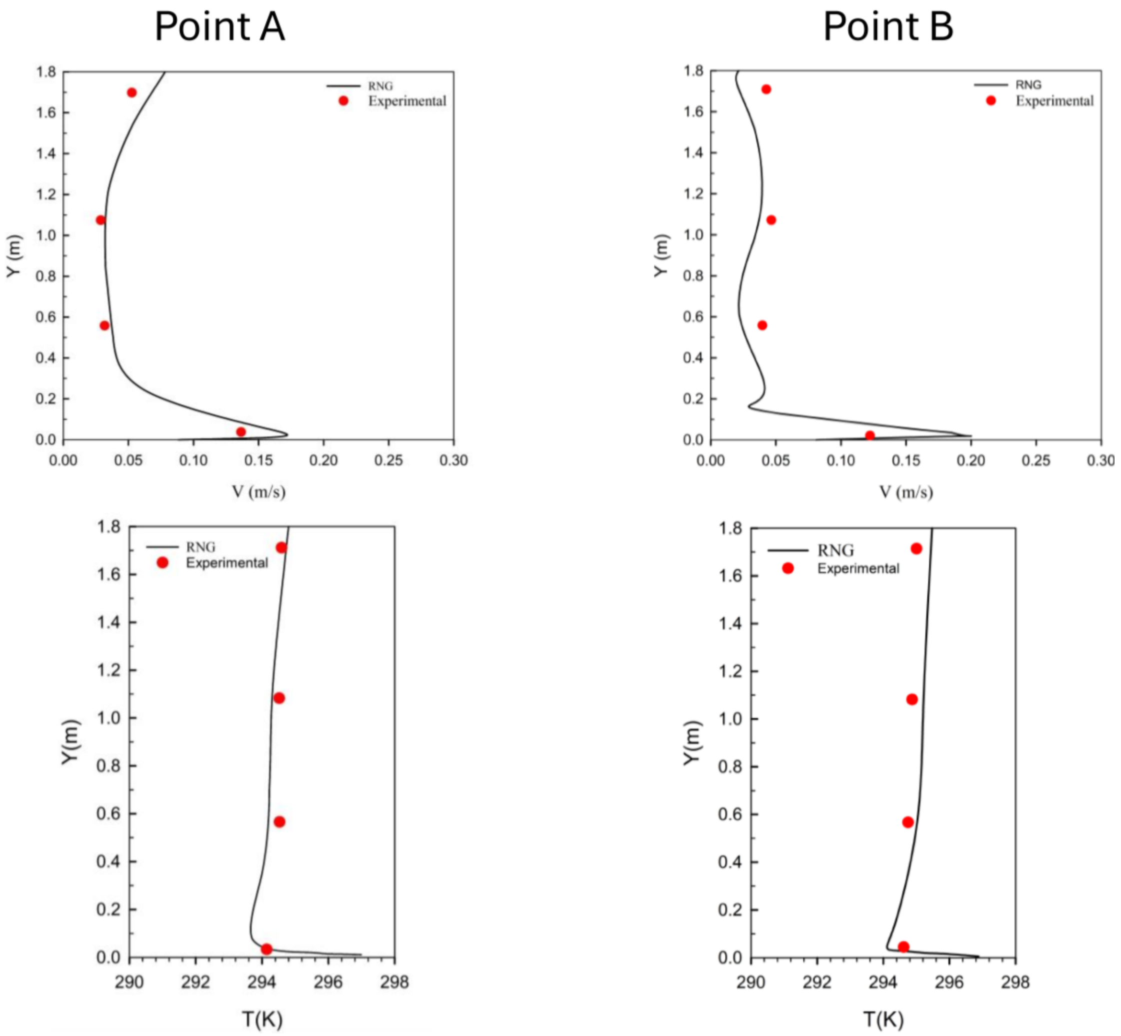

Fig. 3. Comparison of the numerical results with the experimental data [3].

2.5. Optimization

2.5.1. Genetic Algorithm

The genetic algorithm (GA) mimics a natural process to search for the optimal solution for a given problem. The search commences with the generation of an initial set of solutions, known as the population. Each generation of solutions is represented by chromosomes and genes (design variables). Subsequently, over successive generations, a set of modified solutions is produced (over successive generations, the genetic algorithm modifies the genes within chromosomes, generating a new set of solutions in each iteration). The initial solutions are typically modified in such a way that with each generation, the population of solutions converges toward the optimal one. The genetic algorithm leverages the principle of survival of the fittest to navigate the problem-solution space. Chromosomes with higher fitness values have a greater chance of reproducing and contributing to the next generation. After selecting the required number of chromosomes from the preceding generation, two operators, crossover and mutation, can be employed to generate the new generation.

In the realm of multi-objective optimization, the non-dominated sorting genetic algorithm (NSGA-II) is the key method for identifying superior design solutions. This methodology involves constructing a series of Pareto fronts, each representing a set of design points that outperform all other points in terms of all objective functions. The construction of Pareto fronts commences with identifying the initial Pareto front, which comprises all design points that dominate all other points in terms of all objective functions. Domination, in this context, implies that a design point outperforms another in at least one objective function. Once the initial Pareto front is established, the remaining design points are considered. From this set, the second Pareto front is constructed by selecting the design points that dominate all other remaining points in terms of all objective functions. This process continues, with subsequent Pareto fronts being formed by identifying the non-dominated points among the remaining pool of design points. The rank of the Pareto front is inversely proportional to its fitness value. This implies that Pareto fronts with lower numbers represent more desirable design solutions [19, 20]. In the NSGA-II optimization algorithm, the population size is set to 70, with a crossover fraction of 0.8 and a mutation rate of 0.01. The algorithm runs for a maximum of 400 generations. The stopping criteria include a tolerance for the objective function change of 10-4. Additionally, if there is no improvement in the population for 100 consecutive generations, the optimization stops. As discussed previously, the optimization parameters for this problem are the dimensions of the nozzle, the nozzle height, and the supply air mass flow rate. Besides, the objective functions include the predicted percentage of dissatisfaction (PD), the vertical temperature difference, and the total residence time of the resuspended particles, which significantly affect comfort, health, productivity, and efficiency in office environments. The PD index, a crucial factor influencing the local thermal comfort, is calculated at a height of 0.1 m from the floor on the green area shown in Fig.1. Both air velocity and the level of turbulence intensity influence this index:

$$PD = (34 - T)(V - 0.05)^{0.62} (0.37VT_u + 3.14) \tag{23}$$

where V and T are the air speed and temperature, and T_u is the turbulence intensity. The vertical temperature difference, another essential parameter for local thermal comfort, is determined by measuring the temperature difference between two points at different heights (0.1 m and 1.8 m) on the green area shown in Fig.1.

Finally, the total residence time of the resuspended particles in the room, a key objective function for optimizing the indoor air quality, is calculated using the following equation:

$$t_r = \frac{\sum_{i=1}^{n} t_n}{10^6} \tag{24}$$

where t are the residence times of the resuspended particles. This parameter calculates the total residence time of the resuspended particles detached from the ground, excluding those trapped on the surface.

2.5.2. Artificial Neural Network (ANN)

Simplified surrogate models are commonly employed to link problem variables with the objective function. These models reduce the computational cost, making them valuable for solving complex problems. Among the most prominent surrogate models is the artificial neural network (ANN), a powerful technique inspired by the structure and function of the human brain.

An ANN is a sophisticated computational model that learns from data by capturing the intricate relationships between multiple datasets. This knowledge is then stored and utilized to address similar problems in the future. The core of an ANN comprises a vast network of interconnected neurons. These neurons communicate through synapses, which transmit signals from one neuron to another. Following Fig. 4. A schematic of the general characteristics of the artificial neural network, the ANN consists of three distinct layers: an input layer, an output layer, and one or more hidden layers. The input layer receives data from the external environment, while the output layer generates the network's final response. Hidden layers, located between the input and output layers, perform complex computations and extract meaningful features from the data. Each neuron applies a non-linear activation function to the weighted sum of its inputs, enabling the network to model complex relationships. Neurons and synapses are equipped with adjustable weights that are optimized through the learning process [21]. In this study, Bayesian regularization backpropagation is employed to train the neural network. This method is a network training function that updates the weight and bias values according to Levenberg-Marquardt optimization [22]. It minimizes a combination of squared errors and weights and then determines the correct combination to produce a network that generalizes well [23]. So that training can continue until an optimal combination of errors and weights is found. In this study, the neural network model consists of 2 hidden layers with 5 neurons and utilizes the tangent-sigmoid activation function for the hidden layers and the linear activation function for the output one.

2.5.3. Optimization procedure

In this paper, as illustrated in Fig. 5, an ANN is employed to compute the objective functions for solving this problem. The initial dataset for constructing the network is generated using the central composite design (CCD) method [24]. Subsequently, NSGA-II, a multi-objective optimization algorithm, is implemented utilizing the trained ANN. At iterations 25, 50, and 100, the existing ANN is re-trained using the Pareto-optimal solutions obtained at that iteration to minimize the network's error in the vicinity of these optimal points. Additionally, for training, the ANN to better cover areas where the network performance is deemed inadequate; in these iterations, points other than those selected from the Pareto front are also chosen for the training process. Ultimately, upon completion of the aforementioned algorithm, as depicted in Fig. 5, the Pareto-optimal solutions are obtained. This approach enhances the ANN performance in regions proximate to the optimal solutions.

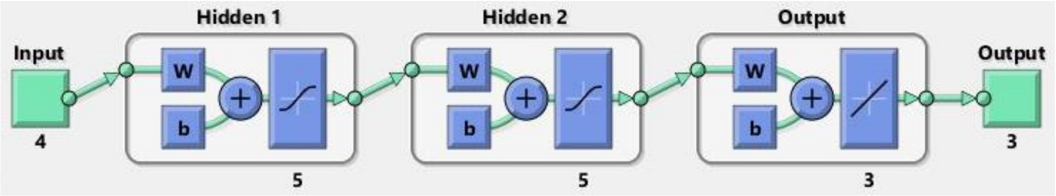

Fig. 4. A schematic of the general characteristics of the artificial neural network

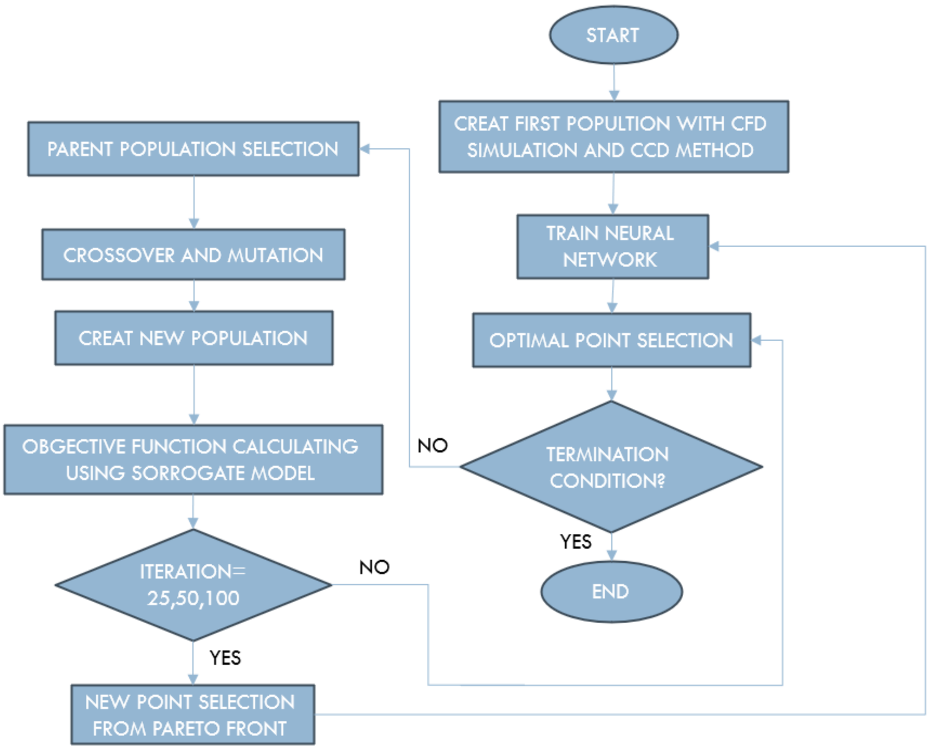

Fig. 5. The optimization procedure flowchart.

3. Results and Discussions

3.1. Factorial analysis

In this section, the full factorial analysis method is employed to investigate the influence of design variables on each objective function. As depicted in Fig. 6, the X-side is the most dominant factor impacting the PD index, with 18% of its overall weight of influence. The mass flow rate takes second place in terms of its impact on the PD index. The results also unveil the intricate interplay between design variables, the pairwise interactions involving height and Z-side dimension, and the mass flow rate and X-side dimension exert more influence on the PD. Figure 7 shows that mass flow rate exerts the most profound influence on the detached particles' residence time, accounting for a substantial 23% of its overall impact. Conversely, height exhibits the least influence among the design variables on the residence time. In addition, among the intricate interplay of design variables, the parameters governing mass flow rate and side dimensions exert the greatest influence on the detached particles' residence time. This analysis suggests that parameters that change the outlet velocity play more significant roles in the residence time.

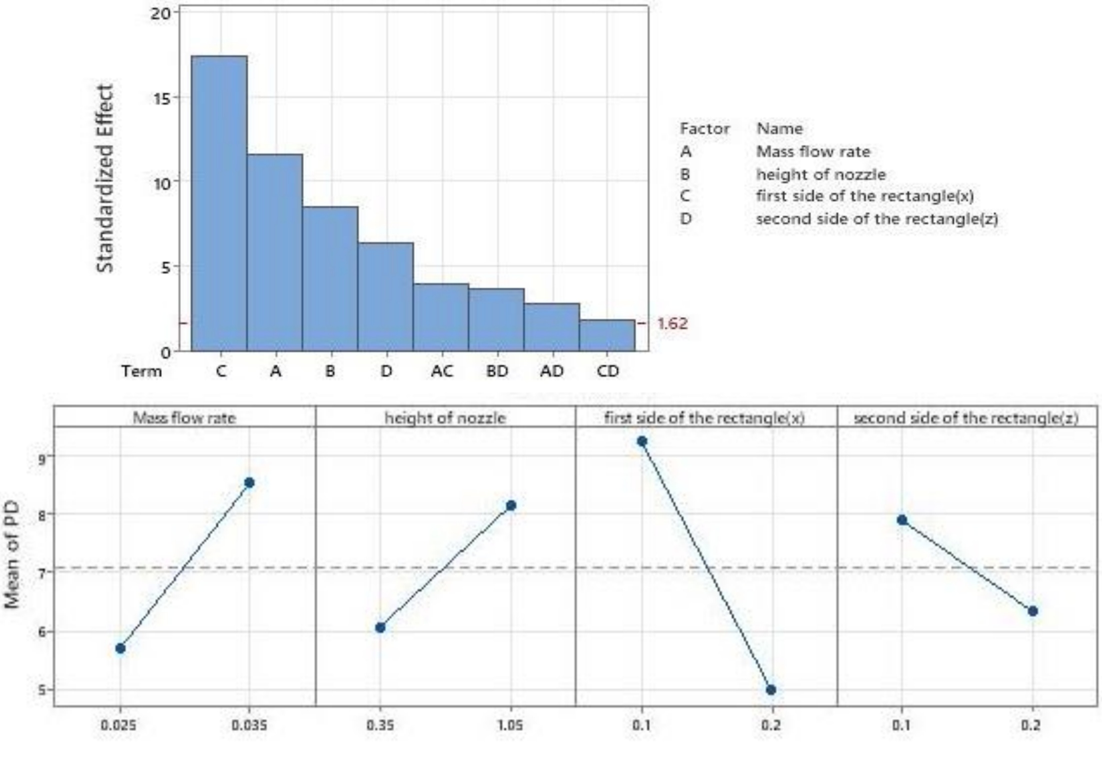

Fig. 6. The effect of design variables on PD.

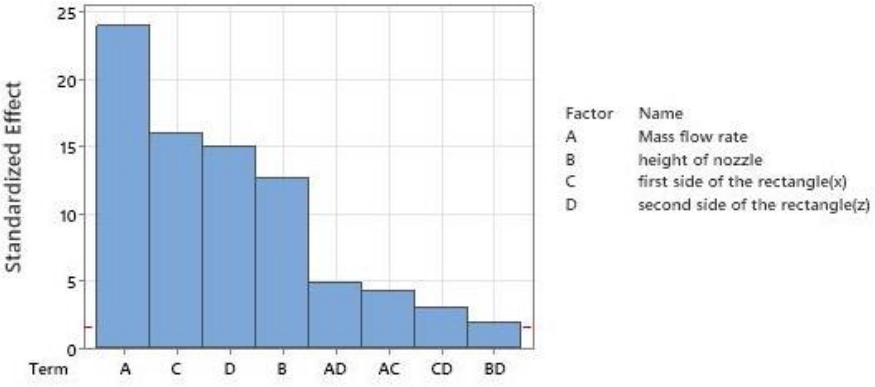

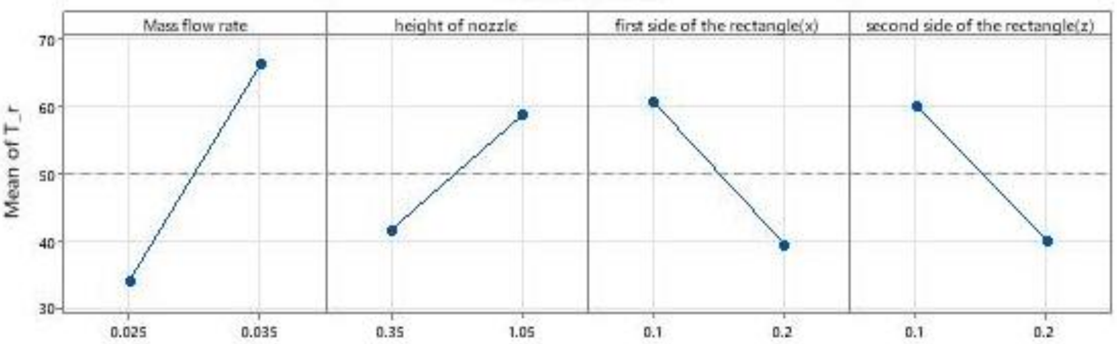

Fig. 7. The effect of design variables on the total residence time of the resuspended particles.

Following Fig. 8, mass flow rate, height, X-side dimension, and Z-side dimension, respectively, with percentages of weights 36%, 22%, 14%, and 10% have the most significant impact on the vertical temperature difference. Moreover, among the intricate interplay of design variables, the interaction between mass flow rate and height exerts the most profound influence on the vertical temperature difference. According to the results, increasing mass flow rate and decreasing nozzle side dimensions, in contrast to the other objective functions of the problem, lead to an increment in the vertical temperature difference. Furthermore, decreasing height has an opposite effect compared to PD and residence time, leading to the vertical temperature difference rise. Based on the results obtained from the full factorial analysis performed on the data obtained from the CCD method, it is evident that all four design variables influence the behavior of the objective functions and, in some cases, act in opposition to each other. Consequently, eliminating any of the design variables would lead to the loss of a portion of the available optimal solutions.

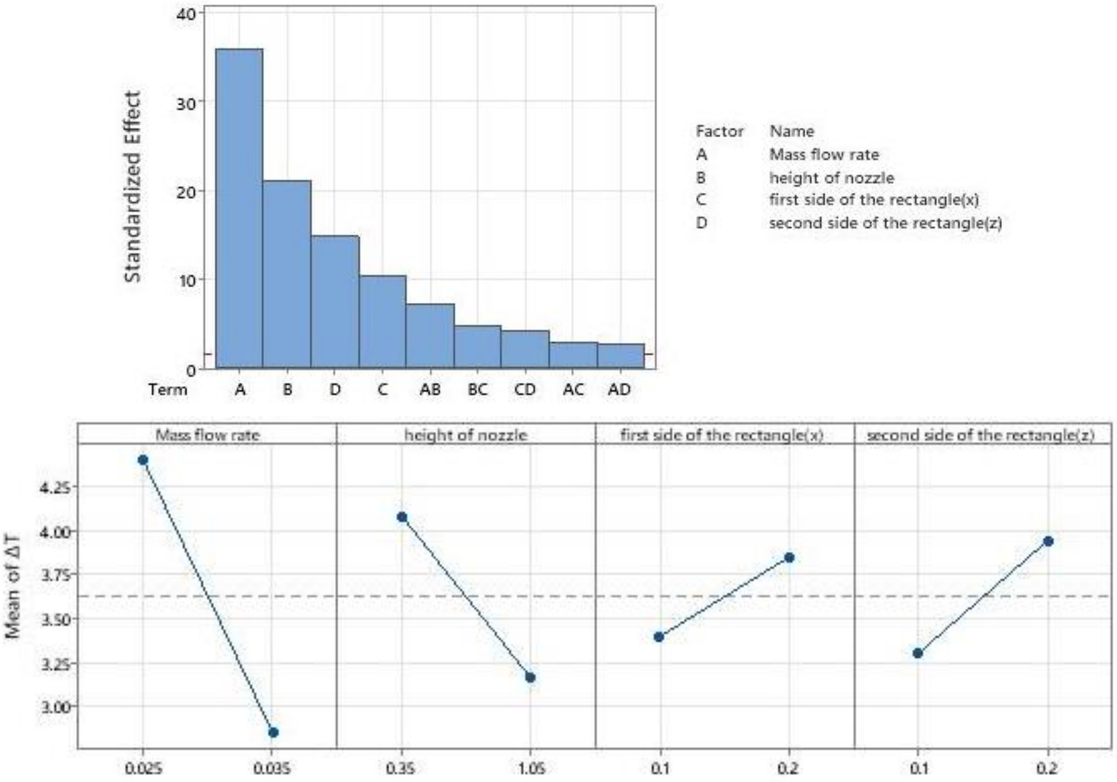

Fig. 8. The effect of design variables on the temperature difference.

3.2. Optimum design

Table 2 presents the values of design variables and their corresponding responses that are used for training the neural network. The initial training phase is performed utilizing the first 25 data points represented in Table 2, extracted from the CCD method. Subsequent lines incorporate a combination of data derived from the Pareto front and random data. Data points 46 and 47 represent the test data for evaluating the neural network.

Table 2 Values of design variables and their responses used to train ANN.

Case	**H (m)**	**$\dot{m}$ (kg s^{-1})**	**X (m)**	**Z (m)**	**PD (-)**	**t_r (s)**	**ΔT (°C)**
1	1.05	0.025	0.10	0.10	9.9	63	3.4
2	1.05	0.035	0.10	0.10	14.2	102	1.8
3	0.35	0.025	0.10	0.10	6.2	40	4.4
4	0.35	0.035	0.10	0.10	10.7	86	2.3
5	0.70	0.030	0.10	0.15	9.0	52	3.7
6	1.05	0.025	0.10	0.20	7.0	36	4.1
7	1.05	0.035	0.10	0.20	10.5	72	2.9
8	0.35	0.025	0.10	0.20	6.2	28	5.0
9	0.35	0.035	0.10	0.20	9.2	58	3.3
10	0.70	0.030	0.15	0.10	7.4	54	3.7
11	1.05	0.030	0.15	0.15	6.6	54	3.5
12	0.70	0.025	0.15	0.15	5.0	28	4.8
13	0.70	0.030	0.15	0.15	5.7	39	4.0
14	0.70	0.035	0.15	0.15	7.7	57	3.3
15	0.35	0.030	0.15	0.15	4.9	35	4.2
16	0.70	0.030	0.15	0.20	5.7	34	4.1
17	1.05	0.025	0.20	0.10	5.0	40	3.6
18	1.05	0.035	0.20	0.10	8.5	75	2.5
19	0.35	0.025	0.20	0.10	3.4	21	5.1
20	0.35	0.035	0.20	0.10	5.2	54	3.2
21	0.70	0.030	0.20	0.15	4.6	33	4.0
22	1.05	0.025	0.20	0.20	4.6	31	4.0
23	1.05	0.035	0.20	0.20	5.5	49	3.0
24	0.35	0.025	0.20	0.20	3.2	13	5.5
25	0.35	0.035	0.20	0.20	4.4	32	3.8
26	1.34	0.040	0.23	0.08	10.3	103	1.5
27	1.48	0.040	0.08	0.08	20.4	137	0.4
28	1.17	0.032	0.25	0.13	5.0	48	3.2
29	1.36	0.039	0.15	0.09	12.5	106	1.4
30	1.21	0.038	0.24	0.12	6.9	68	2.6
31	0.80	0.022	0.21	0.16	3.7	19	4.5
32	0.37	0.038	0.16	0.12	7.6	73	2.7
33	1.00	0.035	0.18	0.09	10.2	82	2.4
34	0.43	0.023	0.20	0.23	2.8	11	5.2
35	0.85	0.039	0.10	0.13	14.0	98	1.9
36	1.18	0.037	0.20	0.13	7.7	68	2.6
37	0.35	0.030	0.10	0.10	8.9	77	3.4
38	0.35	0.030	0.20	0.20	3.8	24	4.3

39	1.35	0.039	0.12	0.10	14.9	116	1.2
40	0.50	0.039	0.21	0.09	6.6	76	2.5
41	1.09	0.035	0.15	0.15	8.4	70	2.7
42	0.35	0.030	0.15	0.20	4.9	28	4.2
43	0.70	0.030	0.10	0.20	7.7	43	3.8
44	0.70	0.025	0.10	0.15	6.6	32	4.1
45	0.37	0.028	0.22	0.17	3.5	18	4.7
46	0.66	0.033	0.26	0.23	4.2	27	4.0
47	0.55	0.023	0.25	0.23	3.2	10	5.3

In Fig. 9, the trained ANN data MSE and test data MSE are shown. According to the result, MSE is 0.016 for training data and 0.03 for test data.

Based on the physical constraints of the problem (shape of the nozzle and its height) and the solutions obtained from the ANN during the training and optimization process, the range of variations for the design variables in the optimization process is summarized in Table 3.

Following optimization of the objective functions derived from the trained ANN using the NSGA-II algorithm, the optimal design points are determined. Among the optimal solutions obtained, any designs corresponding to nozzle shapes that are not manufacturable are removed from consideration. Also, solutions for which an optimization metric reaches its maximum value are excluded from further analysis.

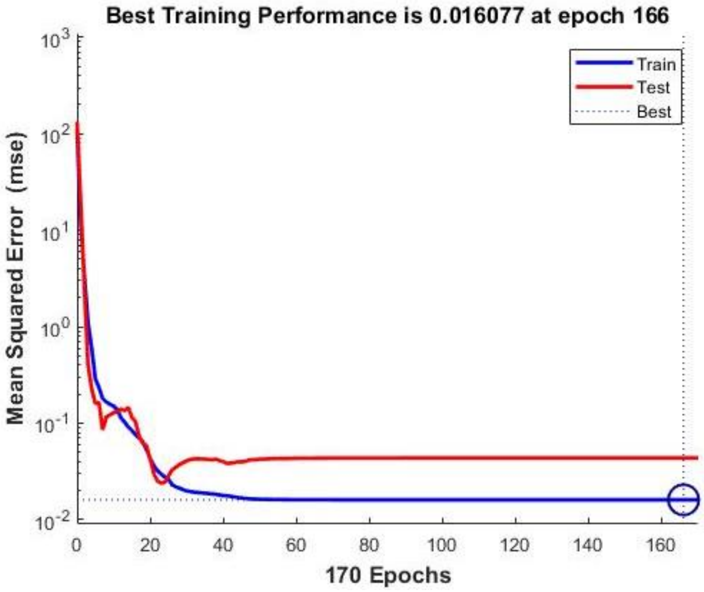

Fig. 9. Evaluation of the trained ANN and test data predictions with CFD data.

Table 3: Low and high levels of design parameters used in the optimization procedure.

Design Parameter	Low Level	High Level
Height (m)	0.30	1.40
X-side dimension (m)	0.08	0.23
Z-side dimension (m)	0.08	0.23
Mass flow rate (kg s^{-1})	0.02	0.04

Figure 10 illustrates the Pareto front for the objective functions of vertical temperature difference and total particle residence time, as well as for vertical temperature difference and PD objective functions. Additionally, Table 4 summarizes the optimal design points extracted from the Pareto front along with their corresponding objective function values. According to ASHRAE standard [25], the vertical temperature difference should not exceed 3°C. Consequently, solutions that fail to meet this criterion are eliminated. The compromise point method [26] is a widely employed approach for selecting the final optimal design point in multi-objective optimization. This method entails selecting the point on the Pareto front that lies closest to the ideal point as the final design point.

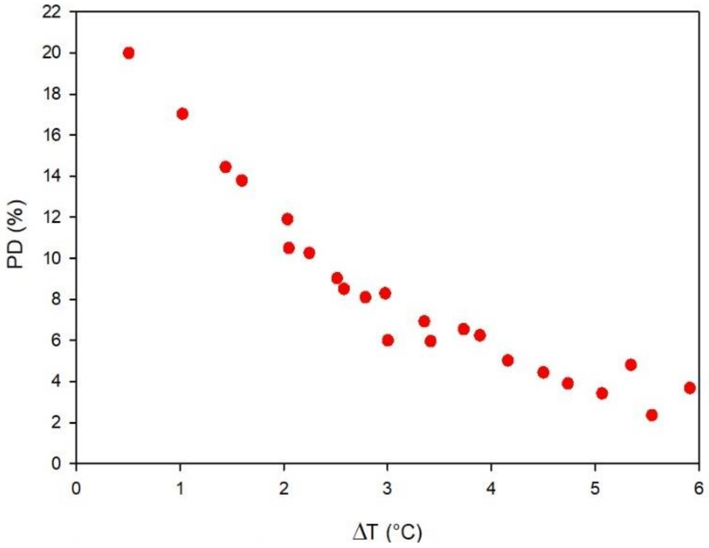

(a) Vertical temperature difference and PD objectives

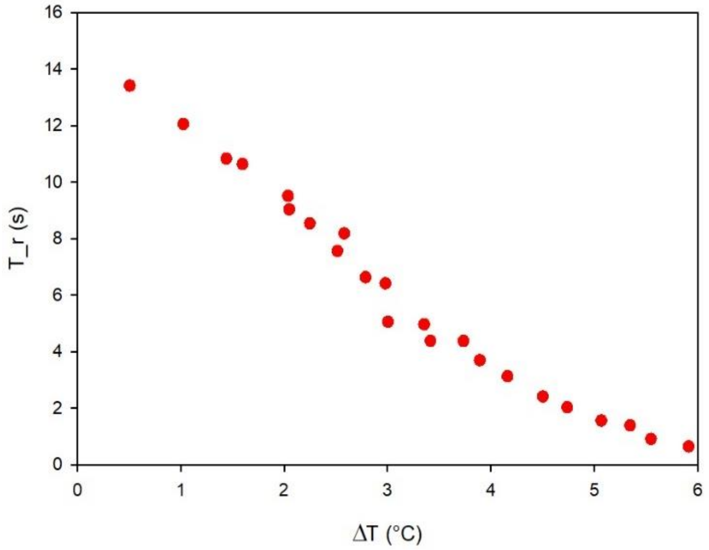

(b) Vertical temperature difference and total particle residence time objectives

Fig. 10. Pareto fronts of the optimum solutions using the coupled ANN/NSGA-II algorithm.

Table 4. Optimal design points and their objective functions.

Case	H (m)	$\dot{m}$ (kg s^{-1})	X (m)	Z (m)	PD (-)	t_r (s)	ΔT (°C)
1	0.31	0.021	0.21	0.21	5.5	0.9	2.4
2	0.39	0.020	0.13	0.23	5.9	0.6	3.7
3	1.39	0.040	0.08	0.09	0.5	13.4	20.0
4	1.32	0.040	0.16	0.16	2.0	9.0	10.5
5	0.63	0.030	0.17	0.18	4.2	3.1	5.0
6	1.26	0.034	0.14	0.15	2.5	7.6	9.0
7	0.56	0.024	0.21	0.20	5.1	1.6	3.4
8	0.39	0.020	0.13	0.23	5.9	0.6	3.7
9	1.39	0.040	0.08	0.09	0.5	13.4	20.0
10	1.40	0.020	0.12	0.20	3.4	4.4	6.0
11	0.60	0.022	0.12	0.19	5.3	1.4	4.8
12	0.72	0.032	0.14	0.16	3.7	4.4	6.5
13	0.74	0.026	0.18	0.18	4.5	2.4	4.4
14	1.25	0.039	0.10	0.12	1.0	12.1	17.0
15	0.97	0.036	0.15	0.16	3.0	6.4	8.3
16	1.19	0.034	0.14	0.17	2.8	6.6	8.1
17	1.15	0.038	0.14	0.13	2.0	9.5	11.9
18	0.70	0.024	0.20	0.18	4.7	2.0	3.9
19	1.32	0.028	0.19	0.16	3	5.1	6
20	1.26	0.022	0.11	0.12	3.4	5.0	6.9
21	1.21	0.040	0.13	0.14	1.6	10.6	13.8
22	1.15	0.040	0.12	0.11	1.4	10.8	14.4
23	1.20	0.022	0.11	0.20	3.9	3.7	6.2
24	1.26	0.037	0.15	0.16	2.2	8.5	10.3
25	0.35	0.037	0.14	0.09	2.6	8.2	8.5

Based on Fig. 10, cases 5, 6, 10, 12, 15, 16, 19, 20, and 23 (see Table 4) are identified as compromise points. The draft index fluctuates between 5% and 9% at the selected points, which is acceptable according to the ASHRAE standard [25]. Also, particles' residence time varies between 3.6 seconds at its lowest and 11 seconds at its highest across the selected points. Among the selected points, cases 5, 10, 12, 13, 20, and 23 are eliminated due to not meeting the 3°C vertical temperature difference constraint. Among cases 6, 15, 16, and 19, which meet the temperature difference criterion, case 19 is expected to perform better due to its lower flow rate leads to lower energy consumption. Case 19 exhibits the best performance among the selected points in terms of the compromise point (having the shortest distance from the coordinate center in the normalized state). However, considering numerical modeling errors and neural network inaccuracies, and given that the vertical temperature difference of case 19 is at the threshold of 3°C constraint, cases 16 and 6 can be selected in terms of the compromise point and energy consumption as the best alternatives in the next step, respectively. Also, case 16 is selected as the optimal design point which corresponds to the nozzle height of 1.19 m, X-side and Z-side dimensions of 0.14 and 0.17 m, respectively, and the mass flow rate of 0.034 kg s^{-1}. This optimum design leads to PD of 8.2, t_r of 6.6 s, and the vertical temperature difference of 2.8°C.

4. Conclusion

In this paper, the JKR particle detachment model was employed to simulate particle resuspension from floor ground due to impinging jet ventilation (IJV) system. The

NSGA-II multi-objective optimization algorithm was used to enhance the performance of the IJV system. The considered design variables were the nozzle side dimensions, height, and mass flow rate. Also, the objective functions were the vertical temperature difference, PD, and the particles' total residence time. To reduce the computational cost associated with evaluating the objective functions, an artificial neural network (ANN) was employed. To reduce the computational error, the ANN neural network was trained in multiple stages.

The results indicated that the mass flow rate exerts the most significant influence on the total particle residence time and vertical temperature difference. Furthermore, it ranks second in terms of its impact on the PD, following the X-side dimension. Increasing the mass flow rate or the nozzle height, or reducing the nozzle side dimensions leads to an enhancement in the PD and total particle residence time, accompanied by a decrement of the vertical temperature difference. Following the optimization process which leads to the Pareto front, the compromise point method was employed to identify the optimal design point which was $X = 0.14$ m, $Z = 0.17$ m, $H = 0.19$ m, and $\dot{m} = 0.034$ kg s^{-1}. In this study, only impingement jet ventilation in the cooling mode was examined, while the heating mode was not considered. Future research could incorporate the heating mode, allowing for the development of optimal design parameters that work effectively in both cooling and heating conditions. This comprehensive approach would ensure that the nozzle delivers optimal performance regardless of the operational mode.

References

[1] Karimipanah T, Awbi H. Theoretical and experimental investigation of impinging jet ventilation and comparison with wall displacement ventilation. Building and Environment. 2002;37(12):1329-42.

[2] Karimpanah T, Sandberg M, Awbi HB. A comparative study of different air distribution systems in a classroom. 2000.

[3] Ye X, Kang Y, Yang F, Zhong K. Comparison study of contaminant distribution and indoor air quality in large-height spaces between impinging jet and mixing ventilation systems in heating mode. Building and Environment. 2019;160:106159.

[4] Chen H, Janbakhsh S, Larsson U, Moshfegh B. Numerical investigation of ventilation performance of different air supply devices in an office environment. Building and Environment. 2015;90:37-50.

[5] Zuo B, Zhong K, Kang Y. An experimental study on particle resuspension in a room with impinging jet ventilation. Building and Environment. 2015;89:48-58.

[6] Haghshenaskashani S, Sajadi B. Evaluation of thermal comfort, IAQ and energy consumption in an impinging jet ventilation (IJV) system with/without ceiling exhaust. Journal of Building Engineering. 2018;18:142-53.

[7] Chen H, Moshfegh B, Cehlin M. Computational investigation on the factors influencing thermal comfort for impinging jet ventilation. Building and Environment. 2013;66:29-41.

[8] Chen H, Moshfegh B, Cehlin M. Investigation on the flow and thermal behavior of impinging jet ventilation systems in an office with different heat loads. Building and Environment. 2013;59:127-44.

[9] Ye X, Kang Y, Zuo B, Zhong K. Study of factors affecting warm air spreading distance in impinging jet ventilation rooms using multiple regression analysis. Building and Environment. 2017;120:1-12.

[10] Haghshenaskashani S, Sajadi B, Cehlin M, editors. Multi-objective optimization of impinging jet ventilation systems: Taguchi-based CFD method. Building Simulation; 2018: Springer.

[11] Wang C, Zhang X, Hu K, Liu Y. Geometric-parameter influence and orthogonal evaluation on the thermal environment for an impinging jet ventilation system inlet. Case Studies in Thermal Engineering. 2023;51:103573.

[12] Li T, Lei J, Luo H, Essah EA, Cheng Y. Parametric study and optimization on exhaled particle dispersion in a ward heated by impinging jet ventilation using orthogonal-based grey relational method.

Journal of Building Engineering. 2024;91:109619.

[13] Fluent A. Ansys fluent theory guide. Ansys Inc, USA. 2011;15317:724-46.

[14] Soltani M, Ahmadi G. Particle detachment from rough surfaces in turbulent flows. The Journal of Adhesion. 1995;51(1-4):105-23, Doi: 10.1080/00218469508009992.

[15] Johnson KL, Kendall K, Roberts A. Surface energy and the contact of elastic solids. Proceedings of the royal society of London A mathematical and physical sciences. 1971;324(1558):301-13.

[16] Soltani M, Ahmadi G. Particle detachment from rough surfaces in turbulent flows. The Journal of Adhesion. 1995;51(1-4):105-23,

[17] Fuller K, Tabor D. The effect of surface roughness on the adhesion of elastic solids. Proceedings of the Royal Society of London A Mathematical and Physical Sciences. 1975;345(1642):327-42.

[18] Greenwood JA, Williamson JP. Contact of nominally flat surfaces. Proceedings of the royal society of London Series a Mathematical and physical sciences. 1966;295(1442):300-19.

[19] Deb K, Pratap A, Agarwal S, Meyarivan T. A fast and elitist multiobjective genetic algorithm: NSGA-II. IEEE transactions on evolutionary computation. 2002;6(2):182-97.

[20] Srinivas N, Deb K. Muiltiobjective optimization using nondominated sorting in genetic algorithms. Evolutionary computation. 1994;2(3):221-48.

[21] Haykin S. Neural networks: a comprehensive foundation: Prentice hall PTR; 1994.

[22] MacKay DJ. Bayesian interpolation. Neural computation. 1992;4(3):415-47.

[23] Foresee FD, Hagan MT, editors. Gauss-Newton approximation to Bayesian learning. Proceedings of international conference on neural networks (ICNN'97); 1997: IEEE.

[24] Cox DR, Reid N. The theory of the design of experiments: Chapman and Hall/CRC; 2000.

[25] ASHRAE (2010). ANSI/ASHRAE Standard 55-2004, Thermal Environmental Conditions for Human Occupancy. American Society of Heating, Refrigerating, and Air-conditioning Engineers, Atlanta

[26] Krus L. Multicriteria decision support in negotiations. Control and Cybernetics. 1996;25:1245-60.